

Generalized Active Disturbance Rejection With Reduced-Order Vector Resonant Control for PMSM Current Disturbances Suppression

Haiyang Cao ^{1b}, Graduate Student Member, IEEE, Yongting Deng ^{1b}, Senior Member, IEEE, Hongwen Li, Member, IEEE, Jianli Wang ^{1b}, Member, IEEE, Xiufeng Liu, Graduate Student Member, IEEE, Zheng Sun, Graduate Student Member, IEEE, and Tian Yang, Graduate Student Member, IEEE

Abstract—A control strategy that combines a novel reduced-order vector resonant controller and a generalized active disturbance rejection control (ROVR-GADRC) is proposed in this article to suppress the current disturbances containing periodic harmonics of a permanent-magnet synchronous motor (PMSM). First, the ROVR controller is designed, which integrates the advantages of both the complex coefficient filter and the vector resonant controller. Compared with the existing resonant control methods, the proposed ROVR can separate and extract the positive and negative sequence harmonics, and avoid the phase delay and peak point simultaneously. Second, a generalized extended state observer is introduced to enhance the suppression of low-frequency disturbance. Then, the composite control strategy is developed. Besides, the stability, disturbance rejection performance, parameters configuration, robustness, and tracking performance of the proposed ROVR-GADRC are comprehensively analyzed. The proposed current controller simultaneously performs harmonics suppression of specific phase sequence and other unknown disturbances attenuation. Finally, the feasibility and effectiveness of the proposed method is verified on a PMSM platform through the experimental results.

Index Terms—Current disturbances suppression, generalized active disturbance rejection control (GADRC), permanent-magnet synchronous motor (PMSM), phase sequence separable, reduced-order vector resonant (ROVR).

Manuscript received 17 October 2022; revised 28 December 2022; accepted 12 January 2023. Date of publication 16 January 2023; date of current version 10 March 2023. This work was supported in part by the National Nature Science Foundation of China under Grants 11973041 and 12122304; and in part by Youth Innovation Promotion Association, Chinese Academy of Science under Grant 2019218. Recommended for publication by Associate Editor N. R. Idris. (Corresponding author: Yongting Deng.)

Haiyang Cao, Jianli Wang, Xiufeng Liu, Zheng Sun, and Tian Yang are with the Changchun Institute of Optics, Fine Mechanics, and Physics, Chinese Academy of Science, Changchun 130033, China, and also with the University of Chinese Academy of Sciences, Beijing 100049, China (e-mail: caohaiyang20@mails.ucas.ac.cn; wangjianli@ciomp.ac.cn; liuxiufeng20@mails.ucas.ac.cn; sunzheng19@mails.ucas.ac.cn; yangtian19@mails.ucas.ac.cn).

Yongting Deng and Hongwen Li are with the Changchun Institute of Optics, Fine Mechanics, and Physics, Chinese Academy of Science, Changchun 130033, China (e-mail: dyt0612@163.com; lihongwen1970@yahoo.com).

Color versions of one or more figures in this article are available at <https://doi.org/10.1109/TPEL.2023.3237331>.

Digital Object Identifier 10.1109/TPEL.2023.3237331

I. INTRODUCTION

PERMANENT-MAGNET synchronous motor (PMSM) is extensively used in advanced servo systems that require high performance and high precision due to high efficiency, high energy density, and convenient maintenance [1], [2], [3]. As the inner loop of the field-oriented control (FOC) structure, the current loop plays a decisive role in the performance of the PMSM [4], [5]. However, the existence of current disturbances deteriorates the dynamic and steady-state performance of the system. Therefore, the current disturbances suppression is significant to achieve high-precision control of the PMSM [6].

Generally, the current disturbances that affect the high-performance PMSM can be classified into two categories. One is the known disturbance, namely cross-coupling terms, which can be eliminated by calculation and compensation. The other is the unknown disturbance, which includes current harmonics, parameters uncertainty, and reference current step change [7], [8]. It is remarkable that the current harmonics are dominated by the low-order harmonic components that contain the -2 nd harmonic introduced by the asymmetric phases [9], [10], and the ± 6 th harmonics caused by the inverter nonlinearity and flux harmonics in the dq -axes [11], [12]. Besides, there are few literatures on dealing with the negative sequence harmonics induced by asymmetric phases.

In order to attenuate the unknown disturbance and improve the system performance, many advanced control strategies have been proposed for the current loop of the PMSM [13], [14], [15]. In these schemes, active disturbance rejection control (ADRC) receives widely attention due to its less dependent on model information, which was proposed by Han in 1990s [16]. In order to promote industrial implementation, a linear ADRC is put forward by Gao [17]. As the core part of ADRC, the extended state observer (ESO) regards parameter uncertainties and external disturbance as a total disturbance and can estimate it in real time, which can be compensated by the feedback control law.

However, the estimation error of the traditional ESO for fast-varying sinusoidal disturbance cannot converge asymptotically [18]. In order to improve the capability of ADRC to suppress periodic current harmonics, there are generally three methods that are increasing observer gain, transforming the

ADRC structure and introducing an auxiliary component. However, a high observer gain will amplify sensor noise while reducing harmonics estimation error [19]. The second approach concentrates on changing the ESO and control law structure to suppress harmonics. To track sinusoidal disturbances, the performance of a generalized ESO (GESO) is analyzed in [20]. It is shown that the capability of a GESO to estimate sinusoidal disturbance is enhanced compared to the traditional ESO. In [21], an adaptive switching GESO is proposed to improve the estimation accuracy and reduce speed ripple. The GESO offers a better estimation effect on low-frequency sinusoidal disturbances, so it is introduced to deal with low-frequency disturbances in this article. However, the GESO has limited effect on suppressing fast-varying harmonics. Thus, it is very necessary to introduce an additional auxiliary component in the ADRC-based scheme.

Consequently, many components combined with ADRC have been proposed to suppress harmonic disturbance, such as iterative learning [22], multiple synchronous rotating frame transformations (MSRFTs) [23] and repetitive controller [24]. In [23], Liu et al. adopt MSRFTs to obtain the primary signals and use closed-loop detection to extract harmonics. In [25], a repetitive control-based ADRC is designed in the discrete-time domain to suppress the sudden and periodic disturbances. Among them, only the MSRFTs can distinguish the positive and negative sequence harmonics. However, the MSRFTs strategy needs twice coordinate transformations and it is difficult for a low-pass filter to completely eliminate the ac component corresponding to the fundamental current. Therefore, new alternative methods need to be found to extract positive and negative sequence harmonics.

Recently, a resonant controller, also known as generalized integrator, has received extensive attention for periodic disturbances suppression [18], [26], [27]. Xia et al. [28] employ a proportional-integral-resonant control method to achieve smooth speed control and utilize switching resonant mode to avoid transient instability. According to the number of integrators, resonant controllers can be divided into two types: second-order and first-order resonant controllers. Traditional resonant (TR) [18], quasi-resonant (QR) [29] and vector resonant (VR) [30] are all second-order resonant controllers. The TR has poor robustness to the controlled signal frequency offset, QR supplements the resonant bandwidth, and VR introduces model information to eliminate the pole of the controlled object. In [27], high-performance resonant controllers with two integrators are implemented, which achieves phase-shift compensation by calculating the target lead angle. However, the second-order resonant controller cannot distinguish between positive and negative sequence harmonics. In addition, there are relatively few research literatures on first-order resonant controller. Li et al. [26] introduce a complex vector proportional integral (PI) (CVPI), which is derived from the reduced order of the TR controller. Wu et al. [31] achieve dead-time compensation for PMSM using complex coefficient filter (CCF). Although the CVPI and CCF can distinguish positive and negative sequence harmonics, they have phase delay and peak point.

Therefore, this article proposes a generalized ADRC (GADRC) with a reduced-order vector resonant controller (ROVR-GADRC) to attenuate the known and unknown

disturbances in the current loop. The proposed ROVR controller integrates the advantages of VR and CCF, which is able to extract phase sequence separated harmonics without phase delay and peak point. The ROVR controller is embedded into the generalized control law and paralleled with the GESO. Meanwhile, the GESO is introduced to suppress low-frequency disturbance and further restrain harmonics. In addition, the performance of the investigated ROVR-GADRC is analyzed in the frequency domain through a two-degree-of-freedom equivalent structure. The main contributions of this article are the following points.

- 1) A novel ROVR controller is proposed to separate and extract the positive and negative sequence harmonics, which avoids phase delay and peak point.
- 2) The proposed ROVR controller is embedded into the generalized control law, which can be tuned independently from the GESO and the control law.
- 3) The proposed ROVR-GADRC can suppress the harmonics of a specific order and phase sequence, and can eliminate other unknown disturbances simultaneously.

The rest of this article is organized as follows. Section II introduces the PMSM dynamic model and analyzes the harmonic components. Section III proposes the ROVR-GADRC for the current loop, and the performance of the ROVR controller and GESO is analyzed. In Section IV, the performances of the proposed method are analyzed. The experiments are carried out to verify the proposed scheme in Section V. Finally, Section VI concludes this article.

II. DYNAMIC MODEL DESCRIPTION AND CURRENT HARMONICS ANALYSIS OF A PMSM

A. Modeling of PMSM Mathematical Dynamics

It is well known that under the condition that the PMSM iron core saturation is ignored and the eddy currents and hysteresis losses are excluded, the mathematical equations of the stator voltage of the PMSM in the dq synchronous rotating reference frame are expressed as

$$\begin{cases} u_{dv} = R_1 i_{dc} + \frac{d\psi_d}{dt} - n_p \omega_m \psi_q \\ u_{qv} = R_1 i_{qc} + \frac{d\psi_q}{dt} + n_p \omega_m \psi_d \end{cases} \quad (1)$$

where $\psi_d = \psi_f + L_d i_{dc}$ and $\psi_q = L_q i_{qc}$ represent the d - and q -axes stator flux linkage, respectively; i_{dc} and u_{dv} denote the stator current and voltage of the d -axis, respectively; i_{qc} and u_{qv} denote the stator current and voltage of the q -axis, respectively; and L_d and L_q are the d - and q -axes inductances of the stator windings, respectively. R_1 is the stator one-phase resistance; n_p represents the motor pole pairs; ω_m is the mechanical angular speed; and ψ_f is the rotor flux linkage. The magnetic circuits of the dq -axes are symmetrical for surface-mounted PMSM, and therefore, $L_d = L_q = L_s$.

Considering the known disturbance and unknown disturbance, and to facilitate the design of the subsequent controllers, (1) can be reconstructed as

$$\begin{cases} \frac{di_{dc}}{dt} = b_0 u_{dv} + f_{dk} + f_d \\ \frac{di_{qc}}{dt} = b_0 u_{qv} + f_{qk} + f_q \end{cases} \quad (2)$$

where $b_0 = 1/L_{s0}$ is the nominal gain of the input current; and f_{dk} and f_{qk} denote the known coupling interferences of d - and q -axes, respectively. Furthermore, f_d and f_q are the d - and q -axes the unknown total interferences, respectively, which contain the internal disturbance $f_{d(q)i}$ caused by parameters perturbation and the external disturbance $f_{d(q)e}$ including harmonics and step change of reference current, i.e., $f_d = f_{di} + f_{de}$ and $f_q = f_{qi} + f_{qe}$. Then, they can be expressed as

$$\begin{cases} f_{dk} = -\frac{R_{10}}{L_{s0}}i_{dc} + n_p\omega_m i_{qc} \\ f_{qk} = -\frac{R_{10}}{L_{s0}}i_{qc} - n_p\omega_m i_{dc} - \frac{n_p\omega_m}{L_{s0}}\psi_{f0} \end{cases} \quad (3)$$

$$\begin{cases} f_{di} = (-\Delta L_s \frac{di_{dc}}{dt} - \Delta R_1 i_{dc} + n_p\omega_m \Delta L_s i_{qc})/L_{s0} \\ f_{qi} = (-\Delta L_s \frac{di_{qc}}{dt} - \Delta R_1 i_{qc} - n_p\omega_m \Delta L_s i_{dc} \\ = -n_p\omega_m \Delta \psi_f)/L_{s0} \end{cases} \quad (4)$$

where $\Delta L_s = L_s - L_{s0}$, $\Delta R_1 = R_1 - R_{10}$, and $\Delta \psi_f = \psi_f - \psi_{f0}$. L_{s0} , R_{10} , and ψ_{f0} are the corresponding nominal values.

B. Current Harmonics Analysis Considering Asymmetric Phases

In the actual operation of a PMSM, the three-phase current is not ideal sine wave, and there will be current harmonics, which will lead to torque and speed fluctuations. Current harmonics include time harmonics and space harmonics, where time harmonics are mainly caused by inverter nonlinearity, while space magnetic field harmonics are related to rotor position such as flux harmonics. However, for the harmonics suppression, there are few literatures that consider asymmetric phases, which is caused by the imbalance of winding parameters between inductance and resistance [10].

The flux harmonics and the voltage harmonics caused by inverter nonlinearity are often modeled and can be found in [25]. According to [9], [10], and [34], the voltage and flux equations of the dq -axes considering asymmetric phases can be expressed as

$$\begin{cases} \frac{d\psi_{dq}}{dt} = \mathbf{u}_{dq} - \mathbf{R}_p \mathbf{i}_{dq} - e^{-j2\omega_e t} \mathbf{R}_n \mathbf{i}_{dq}^* \\ \psi_{dq} = \mathbf{L}_p \mathbf{i}_{dq} + L_s \mathbf{i}_{dq}^* + e^{-j2\omega_e t} \mathbf{L}_n \mathbf{i}_{dq}^* + \psi_f \end{cases} \quad (5)$$

where \mathbf{u}_{dq} , \mathbf{i}_{dq} , and ψ_{dq} are the complex vectors of voltage, current, and flux linkage in the dq -axes; the superscript * denotes the conjugate of the complex vector; \mathbf{R}_p and \mathbf{R}_n are the asymmetric resistance of the positive and negative sequence, respectively; and \mathbf{L}_p and \mathbf{L}_n are the asymmetric inductance of the positive and negative sequence, respectively.

In this article, the fifth and seventh harmonics are mainly considered, which are, respectively, shown as the sixth negative and positive sequence fluctuations in the dq -axes, and the higher harmonics are ignored for that the amplitudes of harmonics decrease with the increase of the harmonic orders [28]. According to (5), the asymmetric phases introduce the -2nd

order harmonic in the dq -axes. Thus, the dq -axes current considering the aforementioned harmonics can be expressed as

$$\begin{cases} i_{dc} = i_{d0} + i_1 \cos(-2\omega_e t + \theta_{i1}) + i_5 \cos(-6\omega_e t + \theta_{i5}) \\ \quad + i_7 \cos(6\omega_e t + \theta_{i7}) \\ i_{qc} = i_{q0} + i_1 \sin(-2\omega_e t + \theta_{i1}) + i_5 \sin(-6\omega_e t + \theta_{i5}) \\ \quad + i_7 \sin(6\omega_e t + \theta_{i7}) \end{cases} \quad (6)$$

where i_{d0} and i_{q0} are the dc components of the dq -axes, respectively; i_1 , i_5 , and i_7 are the first, fifth, and seventh harmonic current amplitudes, respectively; and θ_{i1} , θ_{i5} , and θ_{i7} are the initial phases of the first, fifth, and seventh harmonic currents, respectively. Moreover, $\omega_e = n_p\omega_m$ denotes rotor electrical angular speed.

As shown in (6), the current is mainly affected by the -2nd harmonic and ± 6 th harmonics. Therefore, the proposed algorithm mainly attenuates the -2nd harmonic and the ± 6 th harmonics of the current in the dq -axes.

III. PROPOSED ROVR-GADRC CONTROLLER

In order to suppress the current harmonics and enhance the disturbance rejection capability, this section proposes a ROVR-GADRC controller in the current loop. First, the ROVR controller is proposed and its superiority is analyzed comparatively. Then, a GESO is introduced and analyzed. In the end, the composite control structure is proposed.

A. Design of the ROVR Controller

The VR controller introduces plant information and is an advanced second-order resonant controller [30]. It can be expressed as

$$G_{VR}(s) = \frac{k_{pr}s^2 + k_{ir}s}{s^2 + \omega_c s + \omega_h^2} \quad (7)$$

where k_{pr} and k_{ir} represent the proportional and resonant coefficients, respectively; ω_c is the damping frequency; and ω_h is the resonant frequency.

The CCF controller [31] is a representative of the first-order resonant controller, which can be expressed as

$$G_{CCF}(s) = \frac{k_r \omega_c}{s - j\omega_h + \omega_c} \quad (8)$$

where k_r is the resonant gain and j is an imaginary unit. According to (7) and (8), a novel ROVR controller is proposed by adopting the reduced-order form of CCF and introducing the plant information of VR, which is designed as

$$G_{ROVR}(s) = k_{pr} + \frac{k_{ir} + j\omega_h k_{pr} - \omega_c k_{pr}}{s - j\omega_h + \omega_c} \quad (9)$$

where k_{pr} and k_{ir} are set as

$$\begin{cases} k_{pr} = k_r \omega_c L_{s0} \\ k_{ir} = k_r \omega_c R_{10}. \end{cases} \quad (10)$$

Substituting (10) into (9), the proposed ROVR controller can be expressed as

$$G_{ROVR}(s) = \frac{k_r \omega_c (L_{s0}s + R_{10})}{s - j\omega_h + \omega_c}. \quad (11)$$

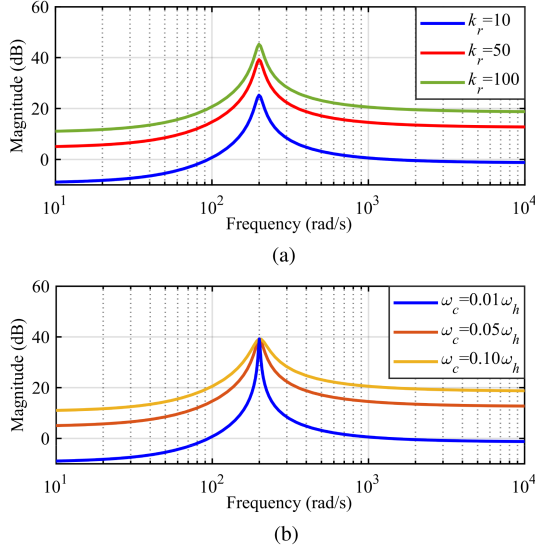


Fig. 1. Bode plot of the ROVR controller for varying parameters. (a) $\omega_c = 0.05\omega_h$, $k_r = [10, 50, 100]$. (b) $k_r = 50$, $\omega_c = [0.01\omega_h, 0.05\omega_h, 0.10\omega_h]$.

To realize the imaginary unit j , we make full use of the orthogonality of the dq -axes, i.e., $u_{dr} = ju_{qr}$ and $u_{qr} = -ju_{dr}$. Let $e_{dc} = i_{dc}^{\text{ref}} - i_{dc}$ and $e_{qc} = i_{qc}^{\text{ref}} - i_{qc}$ be the current deviation inputs, where i_{dc}^{ref} and i_{qc}^{ref} denote reference current in the d - and q -axes, respectively. According to (9), the ROVR controller can be derived as

$$\begin{cases} u_{dr}(s) = \frac{k_{pr}s + k_{ir}}{s + \omega_c} e_{dc}(s) - \frac{\omega_h}{s + \omega_c} u_{qr}(s) \\ u_{qr}(s) = \frac{k_{pr}s + k_{ir}}{s + \omega_c} e_{qc}(s) + \frac{\omega_h}{s + \omega_c} u_{dr}(s) \end{cases} \quad (12)$$

where u_{dr} and u_{qr} are the output voltages of the ROVR controller in the d - and q -axes, respectively. Thus, the complex coefficients are eliminated in (12) for the implementation of the proposed ROVR controller. In this article, the symbol followed by the letter s denotes the frequency-domain signal, otherwise it is the time-domain signal, e.g., $u_{dr}(s)$ and u_{dr} .

In order to illustrate the effect of parameters changes for the performance of the ROVR controller, its bode plot is drawn in Fig. 1 based on (11), where $L_{s0} = 0.0065\text{H}$ and $R_{l0} = 0.675\Omega$. Fig. 1(a) shows that a larger k_r will result in a better harmonics rejection. Moreover, it can be found from Fig. 1(b) that a larger ω_c will increase the bandwidth at the resonant point and improve the robustness to the resonant frequency offset. However, an excessive k_r or ω_c will reduce the dynamic performance and even make the system unstable. Therefore, it is considerable to select appropriate parameters to achieve excellent dynamic performance and harmonics suppression.

The proposed ROVR controller integrates the advantages of VR and CCF controllers, which are listed as follows.

1) The proposed ROVR controller enables the separation and extraction of positive and negative sequence harmonics. The magnitude frequency characteristic curves of VR and ROVR are shown in Fig. 2. It can be seen that the magnitude frequency characteristic of the VR controller has high gain at the resonant frequency ± 100 rad/s and is symmetrical to 0 rad/s. Therefore,

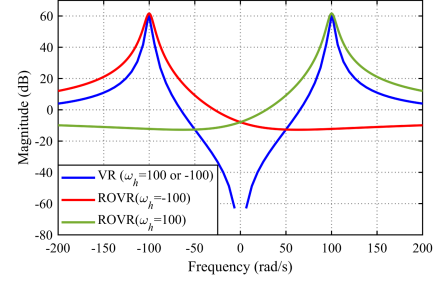


Fig. 2. Magnitude frequency characteristic curves of VR and ROVR.

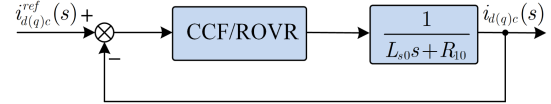


Fig. 3. PMSM current closed-loop structure diagram.

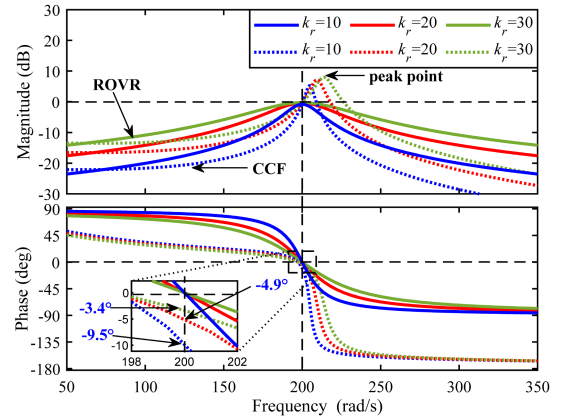


Fig. 4. Bode plot of $G_{cl}(s)$ for two controllers with different k_r values.

the VR controller cannot distinguish between the positive and negative sequence harmonic. In contrast, the ROVR controller has high gain at a specific frequency and small gain at the opposite frequency. Thus, the ROVR controller is more convenient and simpler than the VR controller in extracting the -2nd harmonic caused by the asymmetric phases.

2) The proposed ROVR controller achieves zero-pole cancellation by introducing system model information, thereby avoiding peak point and phase delay. The current closed-loop structure diagram of the PMSM is shown in Fig. 3. Then, the current closed-loop transfer function $G_{cl}(s)$ with the ROVR controller can be derived as

$$G_{cl}(s) = \frac{G_{ROVR}(s)G_P(s)}{1 + G_{ROVR}(s)G_P(s)} = \frac{k_r\omega_c}{s - j\omega_h + (k_r + 1)\omega_c} \quad (13)$$

where $G_P(s) = 1/(L_{s0}s + R_{l0})$ is the simplified current plant of the PMSM.

Fig. 4 shows that the closed-loop bode plots of different k_r values for the ROVR and CCF controller with $\omega_c = 1$ rad/s based on (13). It shows that the ROVR controller can achieve unity-gain and zero-degree phase responses with varying k_r . However,

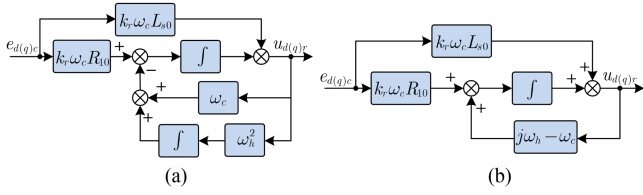


Fig. 5. Structure diagram of VR and ROVR controller. (a) VR controller. (b) ROVR controller.

when k_r is set as 10, 20, and 30, the amplitudes of the CCF have peak points near the resonant frequency, and the corresponding phases are -9.5° , -4.9° , and -3.4° , respectively. Thus, the CCF suffers from phase delay and peak point, which means that the output signal cannot track the input signal well. Although increasing k_r can reduce the phase lag of the CCF, the peak point will be larger and farther away from the resonant frequency. The peak point can amplify the noise near the resonant frequency and even make the system unstable. Therefore, the proposed ROVR can achieve pole-zero cancellation and eliminate peak point and phase delay.

3) The proposed ROVR controller requires relatively less computation. Fig. 5 shows the block diagram of the VR and ROVR controller. It can be seen that two integrators are required to implement the VR controller, while only one integrator is required to implement the ROVR controller. Therefore, the proposed ROVR method has more obvious advantages.

B. Design of the GESO

In order to attenuate the unknown aperiodic disturbance and further suppress the periodic harmonics, a GESO is introduced in this section. Taking the q -axis design as an example, the d -axis design method can be obtained in the same way. Extending the original model with n additional states, (2) can be rewritten as

$$\dot{\mathbf{x}} = \mathbf{A}\mathbf{x} + \mathbf{B}u_{qv} + \mathbf{E}f_q^{(n)} + \mathbf{F}f_{qk} \quad (14)$$

where

$$\mathbf{x} = \begin{bmatrix} i_{qc} & f_q & \dot{f}_q & \cdots & f_q^{(n-1)} \end{bmatrix}_{(n+1) \times 1}^T$$

$$\mathbf{A} = \begin{bmatrix} 0 & 1 & 0 & \cdots & 0 \\ 0 & 0 & 1 & \cdots & 0 \\ \vdots & \vdots & \vdots & \ddots & \vdots \\ 0 & 0 & 0 & \cdots & 1 \\ 0 & 0 & 0 & \cdots & 0 \end{bmatrix}_{(n+1) \times (n+1)}$$

$$\mathbf{B} = [b_0 \ 0 \ 0 \ \cdots \ 0]_{(n+1) \times 1}^T$$

$$\mathbf{E} = [0 \ 0 \ \cdots \ 0 \ 1]_{(n+1) \times 1}^T$$

$$\mathbf{F} = [1 \ 0 \ 0 \ \cdots \ 0]_{(n+1) \times 1}^T$$

Then, the GESO is designed as

$$\begin{cases} e_{q1} = z_1 - x_1 \\ \dot{\mathbf{z}} = \mathbf{A}\mathbf{z} + \mathbf{B}u_{qv} + \mathbf{F}f_{qk} - \mathbf{L}e_{q1} \\ \mathbf{y} = \mathbf{C}\mathbf{z} \end{cases} \quad (15)$$

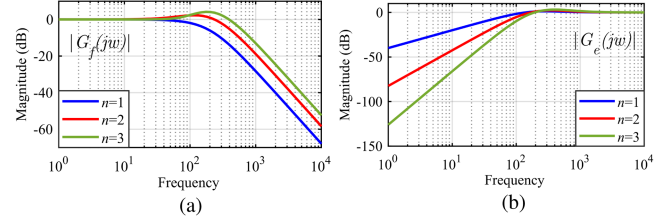


Fig. 6. Bode plots of $G_f(s)$ and $G_e(s)$ at different orders.

where $\mathbf{z} = [z_1 \ z_2 \ \cdots \ z_{n+1}]_{n+1}^T$ represents the estimated vector of \mathbf{x} , $\mathbf{L} = [\beta_1 \ \beta_2 \ \cdots \ \beta_{n+1}]_{n+1}^T$ is the gain vector of the GESO, and $\mathbf{C} = [1 \ 0 \ 0 \ \cdots \ 0]_{n+1}^T$.

$e_q = \mathbf{z} - \mathbf{x}$ is defined to denote the observation error of the GESO. According to (14) and (15), it can be deduced as

$$\dot{e}_q = (\mathbf{A} - \mathbf{L}\mathbf{C})e_q - \mathbf{E}f_q^{(n)}. \quad (16)$$

According to the general observer bandwidth tuning strategy [17], the observer gains are selected as

$$\beta_m = \frac{(n+1)!}{m!(n+1-m)!} \omega_0^m \quad (17)$$

where $m = 1, 2, \dots, n+1$, and ω_0 represents the observer bandwidth. According to (17), the eigenvalues of $(\mathbf{A} - \mathbf{L}\mathbf{C})$ are all negative real numbers and are all configured to $-\omega_0$, in other words, $(\mathbf{A} - \mathbf{L}\mathbf{C})$ is Hurwitz. Meanwhile, if $f_q^{(n)} = 0$, the e_q is asymptotically stable; if $f_q^{(n)} \neq 0$ and it is bounded, the e_q is bounded-input bounded-output (BIBO) stable.

In order to further illustrate the performance of the GESO, the transfer function from z_2 to f_q is derived as

$$G_f(s) = \frac{z_2(s)}{f_q(s)} = 1 - \frac{s^{n+1} + \beta_1 s^n}{(s + \omega_0)^{n+1}}. \quad (18)$$

Then, the transfer function between $e_{q2} = f_q - z_2$ and f_q is shown as

$$G_e(s) = \frac{e_{q2}(s)}{f_q(s)} = \frac{s^{n+1} + \beta_1 s^n}{(s + \omega_0)^{n+1}}. \quad (19)$$

The bode plots of $G_f(s)$ and $G_e(s)$ are shown in Fig. 6 at different orders when ω_0 is fixed. It shows that with the order increases, the low-frequency disturbance rejection performance is enhanced, but the sensor noise is amplified in the high frequency. Therefore, this article selects the second-order GESO to balance the influence of disturbance and noise.

C. Design of the ROVR-GADRC

According to the analysis in Section III-B, the second-order GESO is concretely redesigned by (15) as

$$\begin{cases} e_{q1} = z_1 - x_1 \\ \dot{z}_1 = z_2 + b_0 u_{qv} + f_{qk} - \beta_1 e_{q1} \\ \dot{z}_2 = z_3 - \beta_2 e_{q1} \\ \dot{z}_3 = -\beta_3 e_{q1}. \end{cases} \quad (20)$$

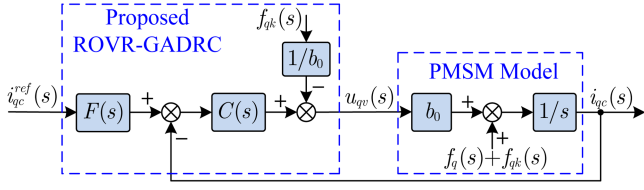
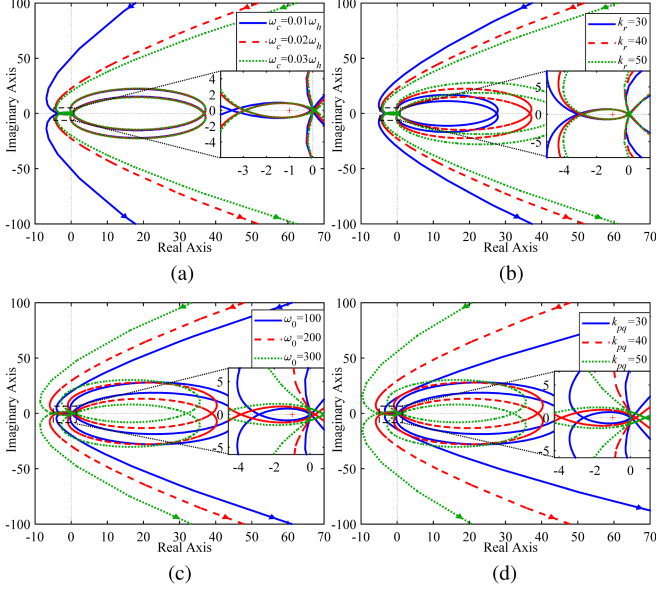


Fig. 8. Equivalent structure block diagram of the ROVR-GADRC.

Fig. 9. Nyquist Diagram of the current loop based on the equivalent model of the ROVR-GADRC. (a) $k_r = 40$; $\omega_0 = 100$; $k_{pq} = 30$. (b) $\omega_c = 0:02\omega_h$; $\omega_0 = 100$; $k_{pq} = 30$. (c) $\omega_c = 0:02\omega_h$; $k_r = 40$; $k_{pq} = 30$. (d) $\omega_c = 0:02\omega_h$; $k_r = 40$; $\omega_0 = 100$.

In Fig. 8, $F(s)$ represents the reference current filter and $C(s)$ is the equivalent controller, which can be expressed as

$$F(s) = \frac{\lambda(s)[Q(s) + s]}{\lambda(s)Q(s) + \beta_2 s^2 + \beta_3 s} \quad (26)$$

$$C(s) = \frac{\lambda(s)Q(s) + \beta_2 s^2 + \beta_3 s}{b_0(s^3 + \beta_1 s^2)}. \quad (27)$$

Then, the open-loop transfer function of the current loop based on the equivalent model of the ROVR-GADRC is given as

$$G_{ol}(s) = C(s)b_0 \frac{1}{s} = \frac{\lambda(s)Q(s) + \beta_2 s^2 + \beta_3 s}{s^4 + \beta_1 s^3}. \quad (28)$$

From (28), the influence of the adjustable parameters ω_c , k_r , ω_0 , and k_{pq} on the stability of the closed-loop system can be analyzed. The Nyquist diagram of the current loop based on the equivalent model of ROVR-GADRC is shown in Fig. 9. The number of open-loop poles in the right half s -plane is zero, and the number of counterclockwise and clockwise circles around the critical point $(-1, 0)$ is equal, so the current closed-loop system based on the ROVR-GADRC is stable. It can be noticed that the changes of the tunable parameters cannot affect the number of turns surrounding the crucial point $(-1, 0)$. Thus, the tunable parameters are weak for the stability of the closed-loop system.

In addition, ω_c and k_r are related to the harmonics suppression characteristic, while ω_0 and k_{pq} have a positive correlation with the rejection performance of the unknown low-frequency disturbance.

B. Antidisturbance Performance of the ROVR-GADRC

To analyze the disturbance rejection capability of the ROVR-GADRC, from Fig. 8 assuming that the current input $i_{qc}^{ref}(s)$ is 0, the transfer function between the current output $i_{qc}(s)$ and the unknown total disturbance $f_q(s)$ is derived as

$$G_d(s) = \frac{i_{qc}(s)}{f_q(s)} = \frac{1/s}{1 + C(s)b_0/s} = \frac{s^3 + \beta_1 s^2}{\lambda(s)Q(s) + s^4 + \beta_1 s^3 + \beta_2 s^2 + \beta_3 s}. \quad (29)$$

The Bode plots of the disturbance transfer functions for the GADRC, CCF-, VR-, and ROVR-GADRC with the same parameters are drawn in Fig. 10. The parameters of the four different controllers are all set to $k_r = 50$, $\omega_c = 10$, $k_{pq} = 50$, and $\omega_0 = 200$. It is found that the high-frequency characteristics of the four controllers are identical, and the low-frequency characteristics have little difference.

In addition, the schemes based on resonant controllers have a considerable amplitude attenuation at the resonant frequency, which indicates that they can suppress harmonics to some extent. The amplitudes of CCF-, VR-, and ROVR-GADRC at the resonant frequency are -73.9 , -88.1 , and -88.1 dB, respectively, which indicates that the latter two have significant harmonics suppression capability. It can also be seen that the CCF-GADRC has a peak point near the resonant frequency, which will amplify the surrounding noise and affect the system performance. Therefore, the proposed ROVR-GADRC has superiority for the PMSM current disturbances suppression.

C. Parameters Configuration

The designed ROVR-GADRC method needs to adjust several parameters, $k_{pq(d)}$, ω_0 , k_{r2} , k_{r6} , ω_{c2} , and ω_{c6} , which affect the stability, robustness, disturbance rejection, and noise suppression performance of the entire system. In order to facilitate engineering application, a simple parameters tuning method is derived according to the steady-state error.

According to Fig. 8, the transfer function from the unknown disturbance to the error can be deduced as

$$G_{fe}(s) = -\frac{s^2 + \beta_1 s}{s^3 + \beta_1 s^2 + \lambda(s)Q(s) + \beta_2 s^2 + \beta_3 s}. \quad (30)$$

According to [4], a disturbance rejection performance measure is introduced, called integrated error (IE), which originates from the effect of step disturbance Δf_q at $t = 0$. Its calculation is expressed as

$$IE = \int_0^{\infty} e dt = L\{e\}_{s=0} = -\lim_{s \rightarrow 0} G_{fe}(s) \frac{\Delta f_q}{s} \quad (31)$$

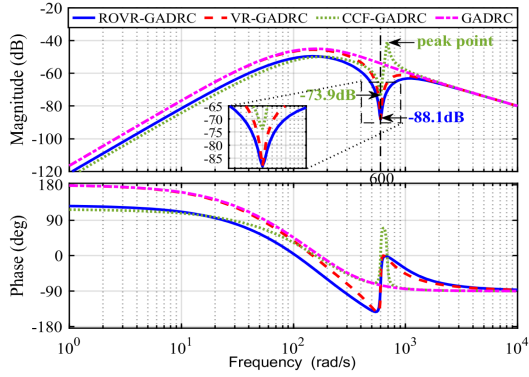


Fig. 10. Bode plots of $G_d(s)$ for four different controllers.

where L is the Laplace transform. Substituting (30) into (31), we can get

$$\text{IE} = \lim_{s \rightarrow 0} \frac{\beta_1}{\beta_3 + k_{pq} + b_0 G'_{\text{ROVR}}(s)}. \quad (32)$$

According to the analysis of Section III-A and [28], the resonant bandwidth ω_c is generally set from 0.1% to 10% ω_h . In this article, let $\omega_{c6} = 2\omega_{c2}$ and $k_{r6} = 2k_{r2}$ couple the relationship of the -2nd and $\pm 6\text{th}$ harmonic suppression parameters. Then, substitute (21) and (22) into (32), IE can be expressed as

$$\text{IE} = \frac{3\omega_0}{\omega_0^3 + k_{pq} + k_{r2}\Gamma} \quad (33)$$

where Γ can be regarded as a constant with a certain range, and its expression is as follows:

$$\begin{cases} \Gamma = \frac{b_0 \omega_{c2} R_{10} (\Gamma_2 \Gamma_3 + 4\Gamma_1 \Gamma_3 + 4\Gamma_1 \Gamma_2)}{\Gamma_1 \Gamma_2 \Gamma_3} \\ \Gamma_1 = -j\omega_{-2} + \omega_{c2} \\ \Gamma_2 = -j\omega_{-6} + \omega_{c6} \\ \Gamma_3 = -j\omega_6 + \omega_{c6}. \end{cases} \quad (34)$$

From (31), it is shown that the smaller IE means the stronger disturbance rejection ability. To get a smaller IE value, k_{pq} and k_{r2} are recommended to set as ω_0 and $\frac{1}{2}\omega_0$, respectively, in this article. Then, (33) can be further simplified as

$$\text{IE} = \frac{6}{2\omega_0^2 + 2 + \Gamma}. \quad (35)$$

Therefore, IE can be reduced by simply increasing ω_0 . However, limited by the current loop bandwidth and noise, ω_0 cannot be increased excessively. In practical engineering, the value of $k_{pq(d)}$ and k_r can be set by selecting ω_0 close to the current loop bandwidth.

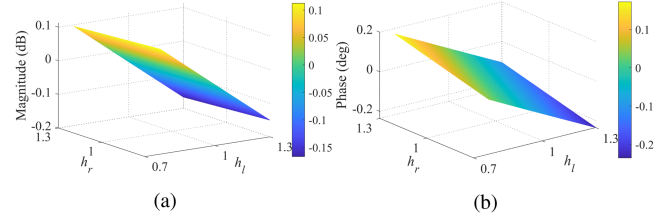


Fig. 11. Amplitude and phase at resonant frequency with PMSM parameters variations.

D. Parameters Robustness Analysis

The inductance L_s and resistance R_1 are affected by temperature changes and aging to produce mismatches from nominal parameters. However, the proposed ROVR-GADRC strategy requires system model information, i.e., L_{s0} , R_{10} , and $b_0 = 1/L_{s0}$. Therefore, it is significant to analyze the robustness of the ROVR-GADRC to parameters mismatch.

From Fig. 8, the current closed-loop transfer function can be derived as

$$G_{cl}(s) = \frac{i_{qc}(s)}{i_{qc}^{\text{ref}}(s)} = \frac{F(s)C(s)}{L_s s + R_1 + C(s)}. \quad (36)$$

Let $h_l = L_s/L_{s0}$ and $h_r = R_1/R_{10}$, and substitute $s = j\omega_h$ into the (36), then (37) shown at the bottom of this page can be obtained.

According to (37), Fig. 11 plots the magnitude and phase at the resonant frequency of the current closed-loop transfer function based on the proposed ROVR-GADRC controller in the presence of mismatch of inductance and resistance. From Fig. 11, it can be seen that the inductance and resistance values vary from 0.7 to 1.3 the nominal values, respectively. The amplitude at the resonant frequency varies from -0.2 to 0.1 dB, which is very close to 0 dB. Meanwhile, the phase varies from -0.2° to 0° , which is also very close to 0° . It can be found that the current closed-loop transfer function maintains unity-gain and zero-phase responses when the model parameters are mismatched. Therefore, the proposed ROVR-GADRC strategy exhibits excellent robustness to parameters variations.

E. Current Reference Command Tracking Performance

In order to illustrate the current reference command tracking performance of different methods, according to (36), the bode plots of the current closed-loop transfer functions for the four different controllers with the same parameters as Section IV-B are drawn in Fig. 12. It can be seen that all four methods can achieve unity gain in the low frequency. When the frequency of the reference command exceeds 200 rad/s of the observer bandwidth, the tracking fluctuations of VR- and ROVR-GADRC are the smallest, and the tracking fluctuation of the GADRC is the largest. The smaller the tracking fluctuation, the better the

$$G_{cl}(j\omega_h) = \frac{\lambda(j\omega_h) [Q(j\omega_h) + j\omega_h]}{\lambda(j\omega_h)Q(j\omega_h) + b_0 h_l L_{s0} \omega_h^4 - b_0 (h_r R_{10} + \beta_1 h_l L_{s0}) j\omega_h^3 - (b_0 \beta_1 R_{10} + \beta_2) \omega_h^2 + \beta_3 j\omega_h}. \quad (37)$$

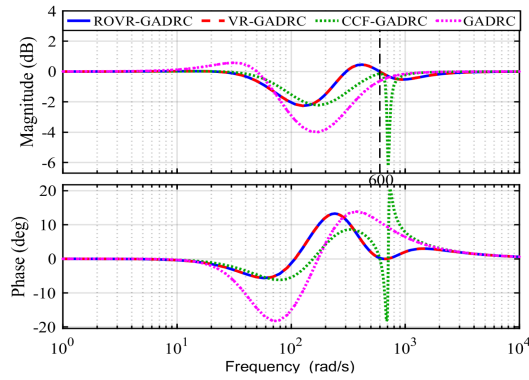


Fig. 12. Bode plots of the current closed-loop transfer function.

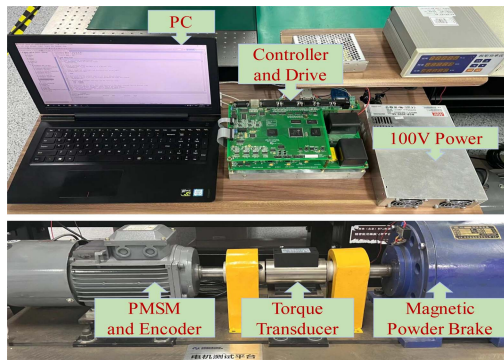


Fig. 13. PMSM experimental test bench.

TABLE I
PARAMETERS OF THE PMSM

Symbol	Quantity	Value	Unit
n_p	Number of pole pairs	3	—
R_1	Stator one-phase resistance	0.675	Ω
L_s	dq -axes inductance	0.0065	H
ψ_f	Rotor flux linkage	0.29	Wb
P_N	Rated power	5.5	kW
I_N	Rated current	5	A
ω_N	Rated speed	600	r/min
U_{dc}	DC-bus rated voltage	100	V

tracking performance. When the frequency is 600 rad/s, VR- and ROVR-GADRC can achieve unity gain and zero-degree phase responses, which means that the vector resonant controller can not only effectively track the disturbance, but also track the current reference command of the corresponding frequency. Therefore, the proposed ROVR-GADRC has relatively superior current reference command tracking performance.

V. EXPERIMENTAL RESULTS

To demonstrate the effectiveness of the proposed ROVR-GADRC strategy, the comparative experiments are performed on a 5.5-kW PMSM hardware platform, as shown in Fig. 13. The main nominal parameters of the PMSM are listed in Table I. In

the experimental setup, the control algorithm is implemented on a DSP-TMS320F28335. A FPGA-EP3C40F324 is employed for analog-to-digital conversion, reading encoder and space vector pulsewidth modulation generation. Besides, the speed loop sampling frequency is 1 kHz and the current loop sampling period 100 μ s. The dead time of pulsewidth modulation is selected as 3 μ s to balance the effect of inverter nonlinearity and asymmetric phases.

The GADRC, CCF-, VR-GADRC, and the proposed control strategy are implemented separately for the current loop of the PMSM to verify the previous analysis. As a matter of fairness, the parameters of ESO and GESO are set to be the same, the control gain $k_{pq} = k_{pd} = 100$ and the observer bandwidth $\omega_0 = 100$, i.e., $\beta_1 = 200$, $\beta_2 = 100^2$, and $\beta_3 = 100^3$. The parameters of the all resonant controllers are selected as $k_{r2} = 50$, $k_{r2} = 100$, $\omega_{c2} = 1$, and $\omega_{c6} = 2$. According to [25], [28], and [29], the current harmonics of the PMSM are more pronounced at the low speed than at the high speed. Hence, the reference speed ω_m^{ref} is determined as 50 r/min in the following experiments.

A. Dynamic- and Steady-State Performance Experiment

In order to comprehensively evaluate the dynamic- and steady-state performance of four different controllers, Figs. 14 and 15 show the comparative experimental results with 3-N-m load and 6-N-m (rated load), respectively. It can be seen from Fig. 14(a) that the steady-state current fluctuations of d - and q -axes with the GADRC are 0.782 and 0.413 A, respectively. Besides, the A-phase current has obvious distortion, and its total harmonic distortion (THD) is 8.63%, and the second and sixth harmonics are the most prominent from the q -axis current fast Fourier transform (FFT) result, which verifies the analysis in Section II-B. Fig. 14(b) shows that the steady-state current fluctuations of dq -axes and the THD of A-phase current are significantly reduced by applying CCF-GADRC, but the amplitudes of specific order harmonics are not completely suppressed according to FFT analysis. With VR-GADRC, it can be found from Fig. 14(c) that dq -axes steady-state current fluctuations are also significantly reduced to 0.235 and 0.246 A, respectively. The THD of the A-phase current is reduced to 1.93%, but the second harmonic is still relatively prominent, because the VR-GADRC cannot distinguish between positive and negative sequence harmonics. Using the proposed ROVR-GADRC, it is found from Fig. 14(d) that the performance of the dq -axes current is further improved. Meanwhile, the THD of the A-phase current is decreased to the minimum value of 1.74%, and the second and sixth harmonic amplitudes also drop to the minimum among the four methods. In addition, the q -axis dynamic response time of the four methods is almost similar, but the methods based on the vector resonant are relatively faster.

The experimental results with rated load in Fig. 15 are consistent with that of the 3-N-m load in Fig. 14. The proposed algorithm is superior to CCF-GADRC in that the former has better capability to suppress the specific order harmonics, which is consistent with the analysis in Section IV-B. Compared with VR-GADRC, the proposed method can well suppress the

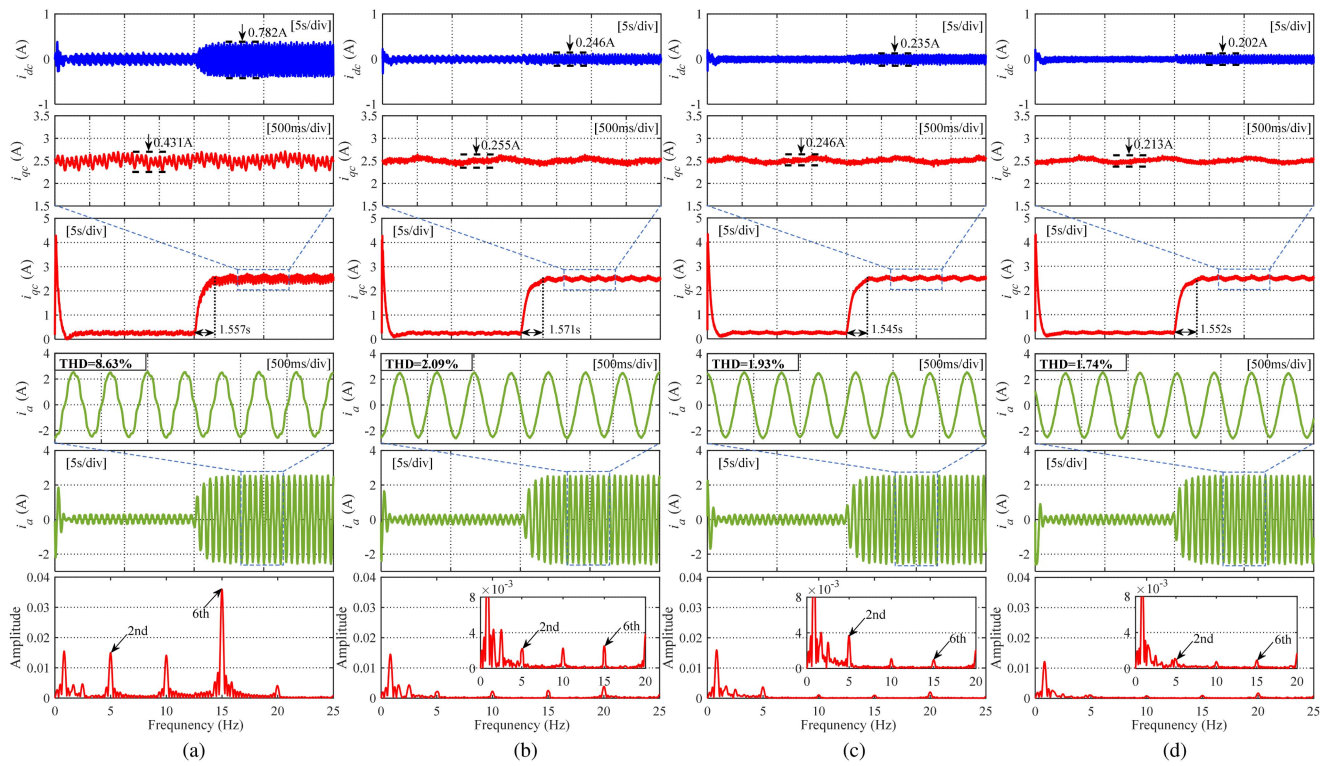


Fig. 14. Experimental results of dq -axes current, A-phase current, and FFT analysis of the q -axis current for four different controllers with 3-N-m load. (a) GADRC. (b) CCF-GADRC. (c) VR-GADRC. (d) ROVR-GADRC.

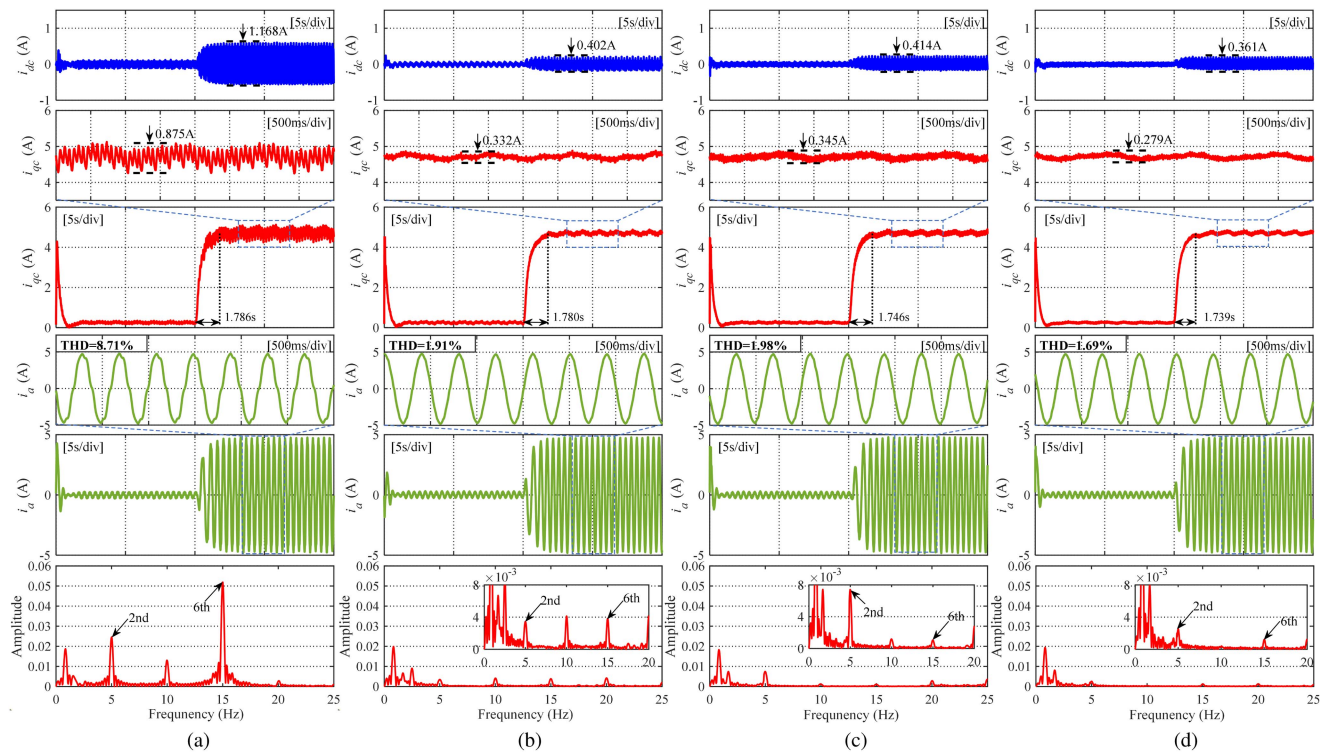


Fig. 15. Experimental results of dq -axes current, A-phase current, and FFT analysis of the q -axis current for four different controllers with rated load. (a) GADRC. (b) CCF-GADRC. (c) VR-GADRC. (d) ROVR-GADRC.

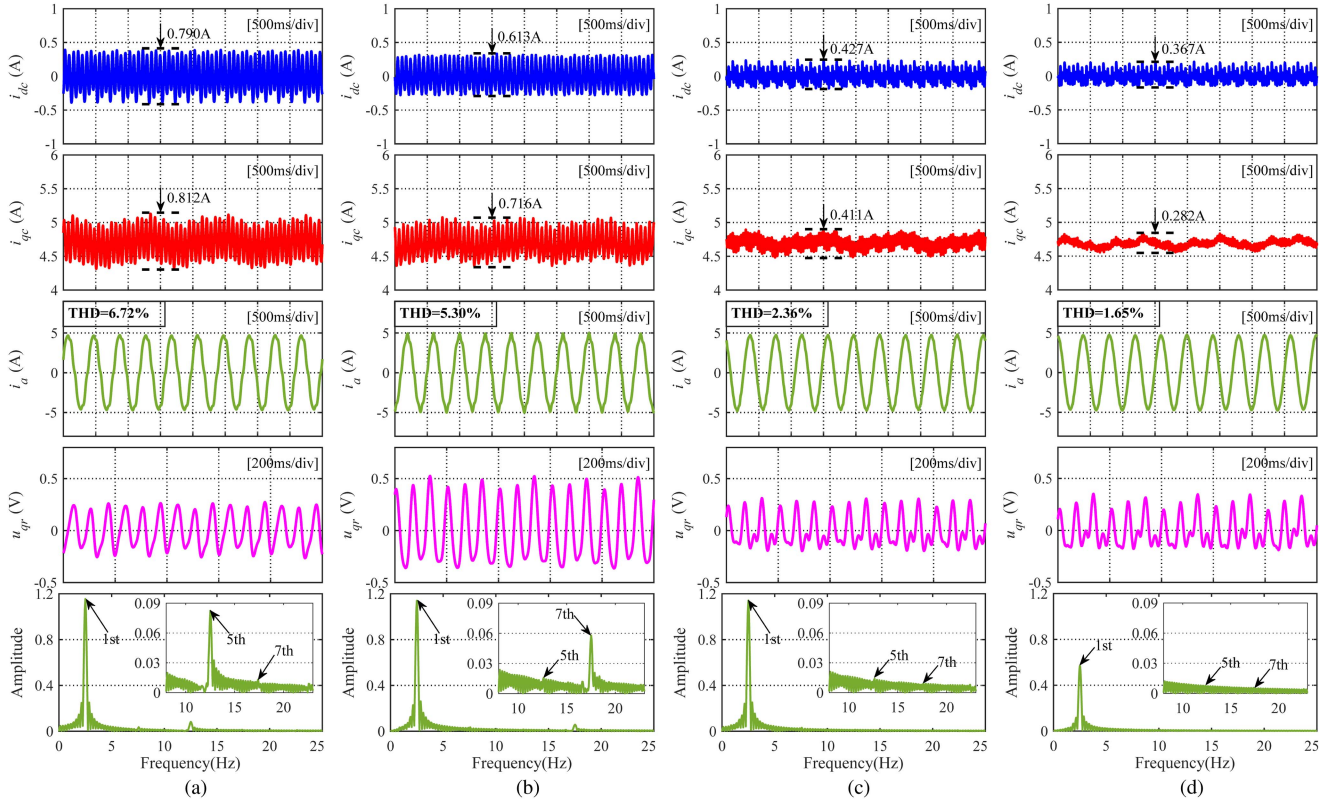


Fig. 16. Experimental results of dq -axes current, A-phase current, output of the ROVR, and FFT analysis of the phase current for the proposed ROVR-GADRC with rated load under different resonant frequencies. (a) $\omega_h = +6\omega_e$. (b) $\omega_h = -6\omega_e$. (c) $\omega_h = \pm 6\omega_e$. (d) $\omega_h = \pm 6\omega_e, -2\omega_e$.

–2nd harmonic caused by asymmetric phases, while VR-GADRC possibly causes fluctuation of the same order and opposite phase sequence. Therefore, the proposed ROVR-GADRC integrates the advantages of CCF- and VR-GADRC, and has better dynamic and steady-state performance.

B. Phase Sequence Separability Experiment

In order to verify that the proposed algorithm has the positive and negative sequence separable property, the resonant frequency ω_h is, respectively, selected as $+6\omega_e$, $-6\omega_e$, $\pm 6\omega_e$, and $\pm 6\omega_e, -2\omega_e$. Fig. 16 illustrates the dq -axes steady-state current, A-phase current, output of the ROVR, and FFT analysis of phase current for the proposed ROVR-GADRC with the rated load under different resonant frequencies.

According to Fig. 15, the THD of GADRC under the rated load is 8.71%. It can be seen from Fig. 16(a) that when $\omega_h = +6\omega_e$, the THD of the phase current drops to 6.72%, and the ROVR controller can extract and compensate the +6th harmonic, so the seventh harmonic of the phase current is basically eliminated. When $\omega_h = -6\omega_e$, the THD is 5.30% in Fig. 16(b), and the –6th harmonic extracted by the ROVR controller is used to compensate the fifth harmonic of the phase current. When $\omega_h = \pm 6\omega_e$ in Fig. 16(c), the d - and q -axes current fluctuations are obviously reduced to 0.427 and 0.411 A, respectively, and the THD is also declined to 2.36%. Besides, the output of the ROVR is a compensation of the

± 6 harmonics to suppress the fifth and seventh harmonics of the phase current caused by inverter nonlinearity and flux harmonics. When $\omega_h = \pm 6\omega_e, -2\omega_e$ in Fig. 16(d), the first harmonic of the phase current caused by the asymmetric phases is also suppressed, and the current waveform is further improved. Therefore, the proposed ROVR-GADRC can well achieve the positive and negative sequence harmonics separation, extraction, and suppression.

C. Robustness Study of Parameters Variation

To verify the robustness of the proposed ROVR-GADRC algorithm, Fig. 17(a)–(c) shows the dq -axes steady-state current and A-phase current of inductance variations, resistance variations, and flux variations, respectively. From (3), (9), and (20), the proposed algorithm involves the effects of inductance, resistance, and flux linkage parameters, which are set as the verification parameters for the robust performance. In the experiment, the nominal parameters of the PMSM are used first, and then, 1.4 and 0.6 times of the nominal parameters are employed, respectively. It can be found from Fig. 17 that the fluctuations of the dq -axes current under the parameters mismatch are essentially consistent with the fluctuations under the nominal parameters, whether it is the inductance, resistance, or flux linkage variations. Besides, the changes of the A-phase current THD are also small and there is no significant distortion of the waveforms. The robustness experiments are consistent

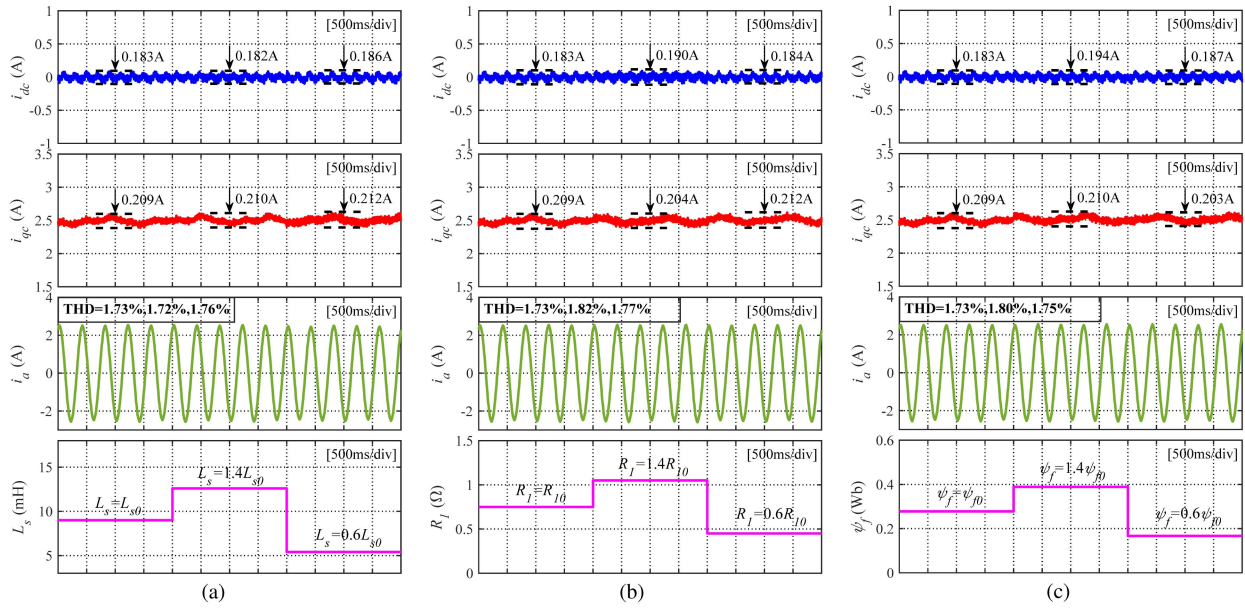


Fig. 17. Experimental results of dq -axes current and A-phase current for the proposed ROVR-GADRC with 3-N-m load under parameters variations. (a) Inductance variations. (b) Resistance variations. (c) Flux linkage variations.

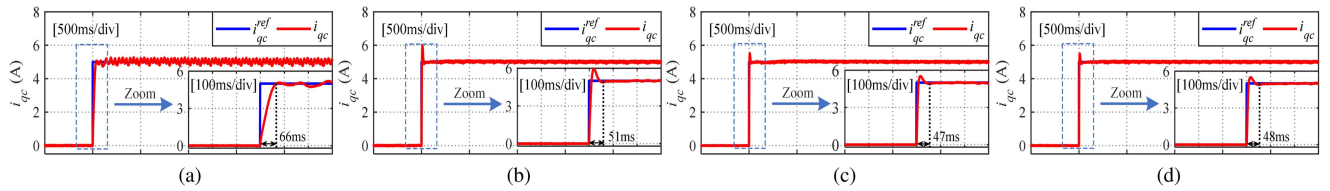


Fig. 18. Experimental results of the q -axis current step response to rated current with four different algorithms with rated load. (a) GADRC. (b) CCF-GADRC. (c) VR-GADRC. (d) ROVR-GADRC.

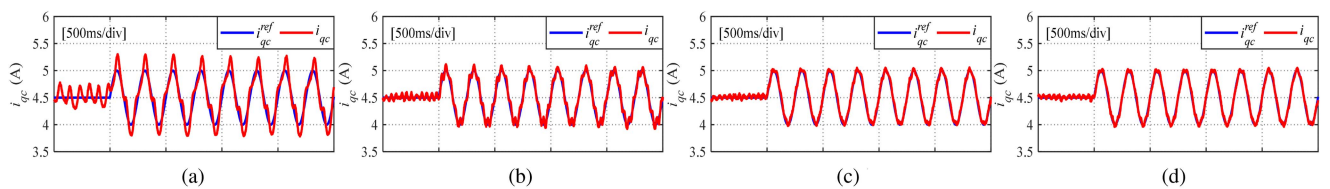


Fig. 19. Experimental results of the q -axis current sinusoidal response with four different algorithms with rated load ($i_{qc}^{ref} = 4.5 + 0.5\sin(8\pi t)$). (a) GADRC. (b) CCF-GADRC. (c) VR-GADRC. (d) ROVR-GADRC.

with the analysis in Section IV-D. Therefore, the investigated ROVR-GADRC strategy is robust to parameters variations.

D. Tracking Study for Step and Sinusoidal References

To illustrate the superior tracking performance of the investigated ROVR-GADRC, Figs. 18 and 19 show the q -axis current responses of four different algorithms to step and sinusoidal signals under rated load, respectively. From Fig. 18, it can be obtained that the step response time of GADRC, CCF-, VR-, and ROVR-GADRC to the rated current is 66, 51, 47, and 48 ms, respectively. Although the resonant controller-based

schemes have relatively fast step response, they suffer from overshoot, which is accordant with the study of [33]. However, the VR- and ROVR-GADRC introduce the model information and reduce the order, which significantly decrease the overshoot amplitude compared with the CCF-GADRC. Furthermore, from Fig. 19, it is evident that the VR- and ROVR-GADRC have the better ability to track the sinusoidal reference among the four algorithms, followed by CCF-GADRC and the worst of GADRC. Therefore, the investigated ROVR-GADRC inherits the excellent tracking performance of the VR-GADRC to the reference current command, which is consistent with the analysis of Section IV-E.

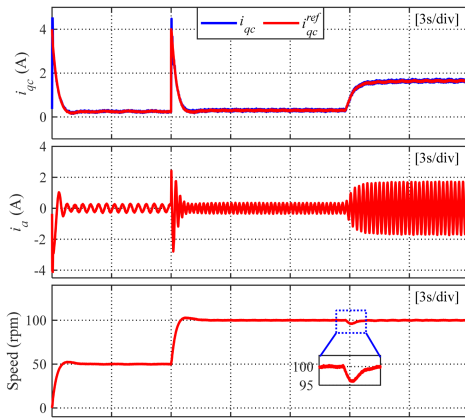


Fig. 20. Experimental results of speed dynamic performance with the reference speed step and 2-N·m load step.

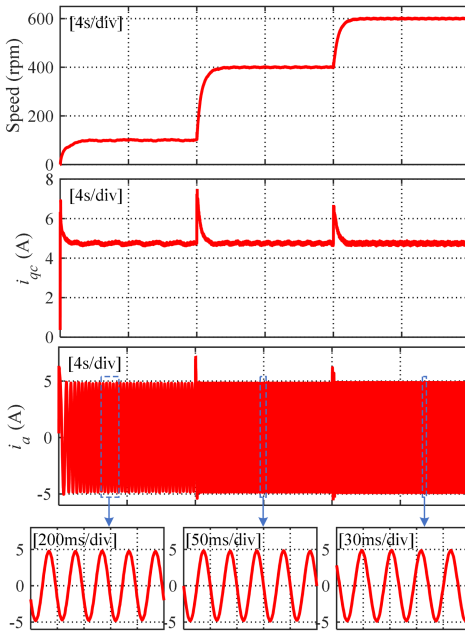


Fig. 21. Experimental results of speed step from low speed to rated speed under rated load.

E. Speed Dynamic Performance Experiment

The proposed ROVR-GADRC adopts a frequency adaptive mechanism to correct the resonant frequency in real time, which is related to the speed. Thus, the speed dynamic performance of the investigated method is experimentally tested. Fig. 20 shows the speed dynamic process for a speed step from 50 to 100 r/min and a load step of 2 N·m, including q -axis current, A-phase current, and speed, from top to bottom, respectively. Fig. 21 shows the speed step from low speed to rated speed under rated load, including speed, q -axis current, A-phase current, and zoom-in A-phase current, from top to bottom, respectively. According to Figs. 20 and 21, it can be found that the q -axis and the A-phase currents fluctuate during the speed step, but the fluctuations disappear quickly as the speed reaches the reference. The q -axis and A-phase currents converge to the corresponding

fixed values during the load step when the speed fluctuation is eliminated. Therefore, the speed dynamic performance of the proposed ROVR-GADRC is verified.

VI. CONCLUSION

In this article, an innovative ROVR-GADRC strategy is investigated to achieve current disturbances rejection of the PMSM. Compared with the existing resonant controller, the proposed ROVR controller realizes the extraction of positive and negative sequence harmonics separately, and eliminates the peak point and phase delay simultaneously, which can suppress the harmonics for smooth current. Meanwhile, a GESO is introduced to further enhance the suppression of low-frequency disturbance. Besides, the stability, disturbance rejection performance, parameters configuration, robustness, and reference command tracking performance of the proposed algorithm are also analyzed. Finally, the performance analysis and experimental results demonstrate that the proposed scheme synthesizes the advantages of both CCF- and VR-GADRC, which has excellent dynamic and steady-state performance, parameters robustness, and tracking capability, and can better suppress negative sequence harmonics. The proposed strategy can also be easily extended to other electric drives.

REFERENCES

- [1] Z. Sun et al., "Finite control set model-free predictive current control of PMSM with two voltage vectors based on ultralocal model," *IEEE Trans. Power Electron.*, vol. 38, no. 1, pp. 776–788, Jan. 2023.
- [2] M. Huang, Y. Deng, H. Li, and J. Wang, "Torque ripple suppression of PMSM using fractional-order vector resonant and robust internal model control," *IEEE Trans. Transport. Electrific.*, vol. 7, no. 3, pp. 1437–1453, Sep. 2021.
- [3] J. Liu, H. Li, and Y. Deng, "Torque ripple minimization of PMSM based on robust ILC via adaptive sliding mode control," *IEEE Trans. Power Electron.*, vol. 33, pp. 3655–3671, Apr. 2018.
- [4] L. Harnefors, S. E. Saarakkala, and M. Hinkkanen, "Speed control of electrical drives using classical control methods," *IEEE Trans. Ind. Appl.*, vol. 49, no. 2, pp. 889–898, Mar./Apr. 2013.
- [5] G. Feng, C. Lai, W. Li, Z. Li, and N. C. Kar, "Dual reference frame based current harmonic minimization for dual three-phase PMSM considering inverter voltage limit," *IEEE Trans. Power Electron.*, vol. 36, no. 7, pp. 8055–8066, Jul. 2021.
- [6] S.-K. Chung, H.-S. Kim, C.-G. Kim, and M.-J. Youn, "A new instantaneous torque control of PM synchronous motor for high-performance direct-drive applications," *IEEE Trans. Power Electron.*, vol. 13, no. 3, pp. 388–400, May 1998.
- [7] S. Kim, W. Lee, M. Rho, and S. Park, "Effective dead-time compensation using a simple vectorial disturbance estimator in PMSM drives," *IEEE Trans. Ind. Electron.*, vol. 57, no. 5, pp. 1609–1614, May 2010.
- [8] D. Lee and J. Ahn, "A simple and direct dead-time effect compensation scheme in PWM-VSI," *IEEE Trans. Ind. Appl.*, vol. 50, no. 5, pp. 3017–3025, Sep./Oct. 2014.
- [9] A. H. Abosh, Z. Q. Zhu, and Y. Ren, "Reduction of torque and flux ripples in space vector modulation-based direct torque control of asymmetric permanent magnet synchronous machine," *IEEE Trans. Power Electron.*, vol. 32, no. 4, pp. 2976–2986, Apr. 2017.
- [10] H. Lin, Y. Liao, L. Yan, F. Li, and Y. Feng, "A novel modulation-based current harmonic control strategy for PMSM considering current measurement error and asymmetric impedance," *IEEE Access*, vol. 10, pp. 89346–89357, 2022.
- [11] V. Petrovic, R. Ortega, and A. M. Stankovic, "Design and implementation of an adaptive controller for torque ripple minimization in PM synchronous motors," *IEEE Trans. Power Electron.*, vol. 15, no. 5, pp. 871–880, Sep. 2000.

- [12] H. Zhu, X. Xiao, and Y. Li, "Torque ripple reduction of the torque predictive control scheme for permanent magnet synchronous motors," *IEEE Trans. Ind. Electron.*, vol. 59, no. 2, pp. 871–877, Feb. 2012.
- [13] Y. Zuo, J. Mei, C. Jiang, X. Yuan, S. Xie, and C. H. T. Lee, "Linear active disturbance rejection controllers for PMSM speed regulation system considering the speed filter," *IEEE Trans. Power Electron.*, vol. 36, no. 12, pp. 14579–14592, Dec. 2021.
- [14] X. Zhang, B. Hou, and Y. Mei, "Deadbeat predictive current control of permanent-magnet synchronous motors with stator current and disturbance observer," *IEEE Trans. Power Electron.*, vol. 32, no. 5, pp. 3818–3834, May 2017.
- [15] P. Lin, Z. Wu, K. -Z. Liu, and X. -M. Sun, "A class of linear-nonlinear switching active disturbance rejection speed and current controllers for PMSM," *IEEE Trans. Power Electron.*, vol. 36, no. 12, pp. 14366–14382, Dec. 2021.
- [16] J. Han, "From PID to active disturbance rejection control," *IEEE Trans. Ind. Electron.*, vol. 56, no. 3, pp. 900–906, Mar. 2009.
- [17] Z. Gao, "Scaling and bandwidth-parameterization based controller tuning," in *Proc. Amer. Control Conf.*, 2003, pp. 4989–4996.
- [18] B. Guo, S. Bacha, M. Alamir, A. Hably, and C. Boudinet, "Generalized integrator-extended state observer with applications to grid-connected converters in the presence of disturbances," *IEEE Trans. Control Syst. Technol.*, vol. 29, no. 2, pp. 744–755, Mar. 2021.
- [19] Z. Yang, Z. Yan, Y. Lu, W. Wang, L. Yu, and Y. Geng, "Double DOF strategy for continuous-wave pulse generator based on extended Kalman filter and adaptive linear active disturbance rejection control," *IEEE Trans. Power Electron.*, vol. 37, no. 2, pp. 1382–1393, Feb. 2022.
- [20] A. A. Godbole, J. P. Kolhe, and S. E. Talole, "Performance analysis of generalized extended state observer in tackling sinusoidal disturbances," *IEEE Trans. Control Syst. Technol.*, vol. 21, no. 6, pp. 2212–2223, Nov. 2013.
- [21] S. Zhu et al., "Robust speed control of electrical drives with reduced ripple using adaptive switching high-order extended state observer," *IEEE Trans. Power Electron.*, vol. 37, no. 2, pp. 2009–2020, Feb. 2022.
- [22] D. Huang, D. Min, Y. Jian, and Y. Li, "Current-cycle iterative learning control for high-precision position tracking of piezoelectric actuator system via active disturbance rejection control for hysteresis compensation," *IEEE Trans. Ind. Electron.*, vol. 67, no. 10, pp. 8680–8690, Oct. 2020.
- [23] G. Liu, B. Chen, K. Wang, and X. Song, "Selective current harmonic suppression for high-speed PMSM based on high-precision harmonic detection method," *IEEE Trans. Ind. Inform.*, vol. 15, no. 6, pp. 3457–3468, Jun. 2019.
- [24] A. H. M. Sayem, Z. Cao, and Z. Man, "Model free ESO-based repetitive control for rejecting periodic and aperiodic disturbances," *IEEE Trans. Ind. Electron.*, vol. 64, no. 4, pp. 3433–3441, Apr. 2017.
- [25] M. Tian, B. Wang, Y. Yu, Q. Dong, and D. Xu, "Discrete-time repetitive control-based ADRC for current loop disturbances suppression of IPMSM drives," *IEEE Trans. Ind. Inform.*, vol. 18, no. 5, pp. 3138–3149, May 2022.
- [26] L. Shuai, S. Lizhi, L. Xingya, and A. Quntao, "Current harmonics suppression strategies of permanent magnet synchronous motor," *Trans. China Electrotechnical Soc.*, vol. 34, no. S1, pp. 87–96, 2019.
- [27] A. G. Yepes, F. D. Freijedo, Ó. Lopez, and J. Doval-Gandoy, "High-Performance digital resonant controllers implemented with two integrators," *IEEE Trans. Power Electron.*, vol. 26, no. 2, pp. 563–576, Feb. 2011.
- [28] C. Xia, B. Ji, and Y. Yan, "Smooth speed control for low-speed high-torque permanent-magnet synchronous motor using proportional-integral-resonant controller," *IEEE Trans. Ind. Electron.*, vol. 62, no. 4, pp. 2123–2134, Apr. 2015.
- [29] B. Wang, M. Tian, Y. Yu, Q. Dong, and D. Xu, "Enhanced ADRC with quasi-resonant control for PMSM speed regulation considering aperiodic and periodic disturbances," *IEEE/ASME Trans. Mechatronics*, vol. 8, no. 3, pp. 3568–3577, Sep. 2022.
- [30] Z. Wang, J. Zhao, L. Wang, M. Li, and Y. Hu, "Combined vector resonant and active disturbance rejection control for PMSLM current harmonic suppression," *IEEE Trans. Ind. Inform.*, vol. 16, no. 9, pp. 5691–5702, Sep. 2020.
- [31] Z. Wu et al., "Dead-time compensation based on a modified multiple complex coefficient filter for permanent magnet synchronous machine drives," *IEEE Trans. Power Electron.*, vol. 36, no. 11, pp. 12979–12989, Nov. 2021.
- [32] H. Jin et al., "On the characteristics of ADRC: A PID interpretation," *Sci. China Inf. Sci.*, vol. 63, pp. 258–260, Oct. 2020.
- [33] Z. Pan, F. Dong, J. Zhao, L. Wang, H. Wang, and Y. Feng, "Combined resonant controller and two-degree-of-freedom PID controller for PMSLM current harmonics suppression," *IEEE Trans. Ind. Electron.*, vol. 65, no. 9, pp. 7558–7568, Sep. 2018.
- [34] A. H. Abosh, Z. -Q. Zhu, and Y. Ren, "Cascaded direct torque control of unbalanced PMSM with low torque and flux ripples," *IEEE Trans. Power Electron.*, vol. 33, no. 2, pp. 1740–1749, Feb. 2018.



Haiyang Cao (Graduate Student Member, IEEE) was born in Shangdong, China, in 1997. He received the B.E. degree in mechanical design, manufacturing, and automation from Northeast Petroleum University, Daqing, China, in 2020. He is currently working toward the Ph.D. degree in mechatronic engineering with the University of Chinese Academy of Sciences, Beijing, China, and the Changchun Institute of Optics, Fine Mechanics and Physics, Chinese Academy of Sciences, Changchun, China.

His main research interests include advanced control theories and applications on motor drive systems.



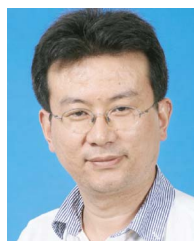
Yongting Deng (Senior Member, IEEE) was born in Shandong, China, in 1987. He received the B.E. degree in automation from the China University of Petroleum, Beijing, China, in 2010, and the M.S. degree in mechatronic engineering and Ph.D. degree in mechatronic engineering from the Changchun Institute of Optics, Fine Mechanics and Physics, Chinese Academy of Sciences, Changchun, China, in 2015.

He is currently a Professor with the Changchun Institute of Optics, Fine Mechanics and Physics, Chinese Academy of Sciences. He has authored or co-authored more than 50 publications in the research interests which include controller design for ac motor drives and linear motor drives, intelligent control, and high-precision machine control techniques.



Hongwen Li (Member, IEEE) was born in Sichuan, China, in 1970. He received the B.E. degree in electrical automation from Sichuan University of Science and Engineering, Zigong, China, in 1993, and the M.S. and Ph.D. degrees in electrical engineering from Jinlin University of Technology, Changchun, China, in 1996 and 2007, respectively.

From 1996 to 2002, he was an Associate Professor with the Jilin University of Technology. Since 2002, he has been with the Changchun Institute of Optics, Fine Mechanics, and Physics, Chinese Academy of Sciences, Changchun, where he is currently a Professor with the Department of Optical-Electronic Detection. His research interests include optical-electric sensor technologies, switching-mode power supply techniques, electric machines and drives, and high-precision machine control techniques. He has authored or co-authored more than 50 publications in these areas.



Jianli Wang (Member, IEEE) was born in Shandong, China, in 1971. He received the Ph.D. degree in mechatronic engineering from the Changchun Institute of Optics, Fine Mechanics and Physics, Chinese Academy of Sciences, Changchun, China, in 2002.

He is currently a Professor with the Changchun Institute of Optics, Fine Mechanics and Physics, Chinese Academy of Sciences. He has authored or co-authored more than 100 publications in his main areas of research, which include optical-electric telescope, high-resolution imaging, and high-precision machine control techniques.



Xiufeng Liu (Graduate Student Member, IEEE) was born in Changchun, China, in 1998. He received the B.E. degree in vehicle engineering from Changchun University of Technology, Changchun, China, in 2020. He is currently pursuing the Ph.D. degree in mechatronic engineering with the University of Chinese Academy of Sciences, Beijing, China, and the Changchun Institute of Optics, Fine Mechanics and Physics, Chinese Academy of Sciences, Changchun, China.

His research interests include ac motor drive, sliding mode control, neural network, and digital control using a digital signal processor.



Tian Yang (Graduate Student Member, IEEE) was born in Hebei, China, in 1996. He received the B.E. degree in mechatronic engineering from Chang'an University, Xi'an, China, in 2019. He is currently working toward the Ph.D. degree in mechatronic engineering with the Changchun Institute of Optics, Fine Mechanics and Physics, Chinese Academy of Sciences, Changchun, China.

His research interests include electric machines and drives and high-precision machine control techniques.



Zheng Sun (Graduate Student Member, IEEE) was born in Henan, China, in 1998. He received the B.E. degree in mechanical design, manufacturing, and automation from Sichuan University, Chengdu, China, in 2019. He is currently working toward the Ph.D. degree in mechatronic engineering with the University of Chinese Academy of Sciences, Beijing, China, and the Changchun Institute of Optics, Fine Mechanics and Physics, Chinese Academy of Sciences, Changchun, China.

His research interests include motor drives, model predictive control, sliding-mode control, and digital control implemented with digital signal processor.